



OPEN

SUBJECT AREAS:

MULTIPHOTON
MICROSCOPY

IMAGING AND SENSING

Received

24 June 2014

Accepted

25 September 2014

Published

15 October 2014

Correspondence and
requests for materials
should be addressed to
P.T.C.S. (ptso@mit.
edu)

Improving femtosecond laser pulse delivery through a hollow core photonic crystal fiber for temporally focused two-photon endomicroscopy

Heejin Choi¹ & Peter T. C. So^{1,2,3,4}

¹Department of Mechanical Engineering, Massachusetts Institute of Technology, Cambridge, MA 02139, USA, ²Department of Biological Engineering, Massachusetts Institute of Technology, Cambridge, MA 02139, USA, ³BioSym, Singapore-MIT Alliance for Research and Technology, Singapore 138602, Singapore, ⁴Laser Biomedical Research Center, Massachusetts Institute of Technology, Cambridge, MA 02139, USA.

In this paper, we present a strategy to improve delivery of femtosecond laser pulses from a regenerative amplifier through a hollow core photonic crystal fiber for temporally focused wide-field two-photon endomicroscopy. For endomicroscope application, wide-field two-photon excitation has the advantage of requiring no scanning in the distal end. However, wide-field two-photon excitation requires peak power that is 10^4 – 10^5 times higher than the point scanning approach corresponding to femtosecond pulses with energy on the order of 1–10 μ J at the specimen plane. The transmission of these high energy pulses through a single mode fiber into the microendoscope is a significant challenge. Two approaches were pursued to partially overcome this limitation. First, a single high energy pulse is split into a train of pulses with energy below the fiber damage threshold better utilizing the available laser energy. Second, stretching the pulse width in time by introducing negative dispersion was shown to have the dual benefit of reducing fiber damage probability and compensating for the positive group velocity dispersion induced by the fiber. With these strategy applied, 11 fold increase in the two photon excitation signal has been demonstrated.

In the last two decades, a number of new biomedical imaging technologies have emerged that fundamentally changed the procedures of disease diagnosis and expanded the frontier of the biological research. For example, two-photon microscopy has now become an indispensable tool for studying brain function and diseases based on the morphological mapping of the neuronal network¹. Optical coherence tomography is routinely used in the diagnosis of retinal diseases such as glaucoma and age related macular degeneration². More recently, photoacoustic tomography has demonstrated potential in in-vivo monitoring of the tumor angiogenesis³.

Multiphoton microscopy is one of these powerful biomedical imaging modalities that can provide both morphological and spectroscopic information on tissue states based on endogenous fluorophores signals. For example, cancer cells often has distinctive morphological features during carcinogenic progression such as an increase in nuclear to cytoplasmic ratio. Spectroscopically, a decrease in the redox ratio of the metabolic coenzyme FAD and NADH has been observed^{4,5}. Multiphoton microscopy can also utilize second harmonic generation (SHG) to monitor collagen conformation in the extracellular matrix. Recent studies have shown that SHG can be a useful diagnostic marker for muscular dystrophy and ovarian cancer⁶ and can provide a diagnostic index for liver fibrosis progression⁷ and cervical remodeling during pregnancy⁸. For these reasons, the development of multiphoton endomicroscopy may find use as an optical biopsy tool for diagnosing diseases such as colorectal, esophageal, and cervical cancer which occurs on epithelial surface of body cavities and can only be reached with a miniaturized device.

Although multiphoton endomicroscopy is a promising technology, its miniaturization is technically challenging because it typically requires the 3D beam scanning mechanism to be installed at the distal end of the device^{9–14}. Further, the point scanning procedure results in an image acquisition process that is inherently slow. These problems can be circumvented by utilizing the temporally focused two photon microscopy (TFM) that can significantly reduce instrument complexity and can offer the potential for higher speed imaging based on parallelization by producing a depth resolved wide field images without the need for scanning mechanisms at



the distal end^{15,16}. Axial scanning can also be performed remotely by chirping excitation pulses in the proximal end¹⁷. However, the application of TFM for endomicroscopy has a number of inherent difficulties. TFM requires high peak power pulses from a regenerative amplifier to efficiently excite the whole field-of-view¹⁸. However, the use of high energy pulses is a challenge for endomicroscope design because laser light must be delivered by fiber optics that is readily damaged at these energy levels.

In this paper, we propose a strategy to improve high energy pulse delivery through a hollow core photonic crystal fiber (HCPCF) by manipulating laser peak power with a compact pulse splitter and laser group velocity dispersion with a pulse compressor. We demonstrate that the excitation efficiency of a temporally focused wide-field two photon endomicroscope (TFEM) can be substantially improved.

Methods

Improving the two photon excited fluorescence signal using pulse splitter. Light guidance by the standard step index fiber is based on total internal reflection between the higher refractive index core and the lower index cladding. However, these solid core fibers are not optimal for delivering high peak power pulses because of temporal distortions induced by nonlinear processes, such as self-phase modulation and group velocity dispersion (GVD), in the core material. On the other hand, light can be trapped inside the air core of HCPCFs based either on the photonic band gap effect¹⁹ or the inhibited coupling guidance²⁰. Since light propagates mostly through air, temporal distortion of these pulses is minimized²¹. HCPCF have been utilized for delivering high peak power pulses for various applications including two photon fluorescence microscopy²², laser micromachining²³ and laser surgery²⁴.

While two-photon laser scanning microscopy (TPLSM) requires 0.01–0.1 nJ pulse energy from a Ti-sapphire laser to achieve optimal excitation efficiency, TFM requires 10^4 – 10^5 times higher pulse energy due to the need to completely cover even a modest field-of-view ($>100 \times 100 \mu\text{m}^2$). Considering the power loss during beam delivery through the optical fiber and the intermediate optical elements, even the full power from a Ti-sapphire laser is often insufficient. This limitation was overcome in a TFM using a regeneratively amplified Ti-sapphire laser with μJ or mJ level peak power¹⁸. However, for TFEM, a major challenge is the delivery of these high peak power pulses through an optical fiber without thermal or ionization damage.

Figure 1 shows a flat cleaved surface of HCPCF (HC-800-01, NKT photonics) and a surface damaged by the high peak power pulses from a regeneratively amplified Ti-sapphire laser operating at 800 nm wavelength with 8 nm spectral width, 130 fsec pulse width, and 10 kHz repetition rate (Legend Elite, Coherent). The damage of HCPCF mostly occurs at the inlet of the fiber when the focused beam spot size and shape does not match with the mode field of the HCPCF. The maximum transmittable power is closely related to the coupling efficiency. If the coupling is not optimal, fiber damage often occurs before the absolute maximum value set by material damage threshold.

There are several factors that determine the coupling efficiency including the flatness of the cleaved surface, the input beam diameter, the numerical aperture (NA) of the coupling lens, the NA of the fiber, and the size of the fiber mode diameter. The rule of thumb for maximizing the coupling efficiency is that the NA of the focused beam should be less than the NA of the fiber. At the same time, the focused beam spot size should be less than the size of the core diameter. The HCPCF (HC-800-01, NKT photonics) used for delivering the pulses from the regenerative amplifier had a NA of 0.2, a mode field diameter ($1/e^2$ width) of 8.8 μm and a zero dispersion wavelength near 805 nm.

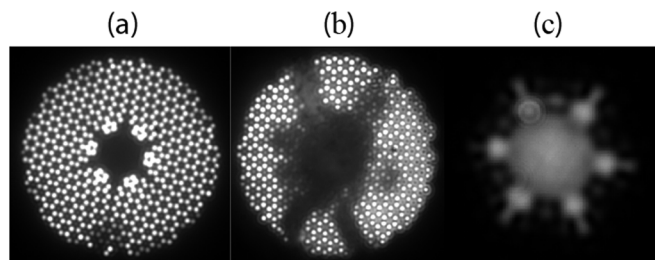


Figure 1 | Far field image of the end surface of HC-800-01 fiber (a) clean surface (b) damaged surface. These images are acquired by illuminating the proximal end of the fiber with a white light LED and imaging the distal end with a $40\times$ air objective and a CCD camera. The bright dot shown is the photonic lattice structure where the light from LED propagate through these structures via total internal reflection (c) intensity pattern of the output beam from the hollow core fiber.

The damage threshold of the fiber was measured by increasing the input pulse energy to the fiber at 20 nJ intervals until damage. The pulse energy from the regenerative amplifier was controlled by using a half wave plate (10RP02-800, Newport) and a polarizer (GL15-B, Thorlabs). First, the output beam diameter from the regenerative amplifier was reduced to the aperture size of the coupling lens using a telescope and then it was coupled to the fiber using an aspheric lens with NA of 0.16 (C260TME-B, Thorlabs). The optimal coupling lens had been selected after trying several choices with NA varying from 0.15 to 0.25. With the 0.16 NA coupling lens, coupling efficiency up to 90% had been achieved. Fiber damage often occurred sequentially. Coupling efficiency remained constant up to about 360 nJ input pulse energy and then started to drop slowly as cracks developed in the core. At some point, the transmitted power decreased abruptly with the total destruction of the core as shown in Fig. 2. The fiber damage by the ionization effect can be avoided by coupling in and out of the fiber within the vacuum chamber minimizing damage due to air ionization. In this condition, femtosecond pulses with energy up to 1.8 μJ was transmitted through HCPCF without damage²⁵. More recently, helium gas filled kagome-type HCPCF was shown to deliver 1550 nm sub-picosecond pulses up to 74 μJ ²⁶ although the bulky vacuum coupling at the distal limits its endoscopic uses²⁷.

For the optimal widefield two-photon excitation, 1–10 μJ pulse energy is required. Although, regenerative amplifiers can provide high energy pulses that satisfy this requirement, these pulses cannot be delivered to the distal end effectively due to fiber damage. Instead of just attenuating the laser pulse peak power, one approach to better utilize the power of the regenerative amplifier is to split each regeneratively amplified pulse into multiple pulses. In this way, it is possible to increase the number of available pulses for two photon excitation while keeping pulse energy below fiber damage threshold. Theoretically, two photon absorption (TPA) per fluorophore per second can be expressed as Eq. (1).

$$TPA = \delta \left(\frac{\lambda}{hc} \right)^2 \frac{1}{FOV^2} P_{peak}^2 \tau f = \delta \left(\frac{\lambda}{hc} \right)^2 \frac{1}{FOV^2} \frac{e_{pulse}^2}{\tau} f \quad (1)$$

where δ is TPA cross-section, λ is the wavelength, c is the speed of light, h is the Planck constant, P_{peak} is the peak power of pulse, e_{pulse} is the pulse energy, f is the pulse repetition rate, τ is the pulse width and FOV is the illumination field of view¹. Eq.(1) implies that the signal in TFEM can be maximized by setting the pulse energy (peak power) below the fiber damage threshold and by increasing the number of pulses as many as possible. In a sense, this is similar to an optimization problem where the objective function is TPA and the optimization parameters are pulse energy and repetition rate with the fiber damage threshold acting as a constraint. Our solution was to implement a pulse splitter that multiplies the incoming pulse to many identical pulses while keeping the peak power of each pulse below the damage threshold. This pulse division approach also had been utilized for the femtosecond fiber amplification process²⁸.

Figure 3 shows the pulse splitter design that multiplies an incoming pulse to 64 identical pulses with a timing diagram showing the pulses at some intermediate steps. The detail design was adapted from the work of Ji et al²⁹. To summarize the sequence of pulse multiplication steps, the pulse was split into two by a non-polarizing beam splitter (BS₁). One of these pulses went to PS₁ directly and the other was delayed by delay line (l₁) and sent to the other input port of PS₁. Each input pulse to PS₁ was multiplied to 4 pulses by a $4\times$ pulse splitter where the two pulses from each output ports were time delayed by 74 ps. Pulses from one of the output ports of PS₁ was delayed by delay line, l₂, and recombined with pulses from the other output ports of PS₁ at BS₂. BS₂ split these pulses to two sets of pulses. One group of pulses went directly to PS₂ and the other group of pulses went to delay line, DL, which added about 2.5 ns time delay before the pulses entered the other input port of PS₂. Each input pulse to PS₂ was multiplied to 4 pulses by the $4\times$ pulse splitter where the two pulses from each output ports were time delayed by 37 ps. Pulses from one of the output ports of PS₂ was delayed by a delay line, l₃, and recombined with pulses from the other output ports of PS₂ using half-wave plate (HWP) and polarizing beam cube splitter (BS₃). The time delayed pulses in PS₁ and PS₂ were produced by splitting the input pulses at the interface of the two different refractive index materials so that each pulse

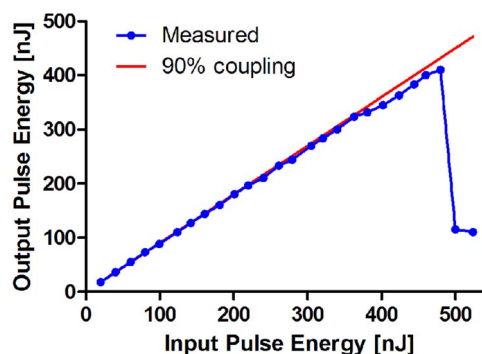


Figure 2 | Coupling efficiency plot of HC800-01 fiber. The pulse energy from the regenerative amplifier with 10 kHz is incrementally increased until the output pulse energy deviate the constant coupling efficiency.

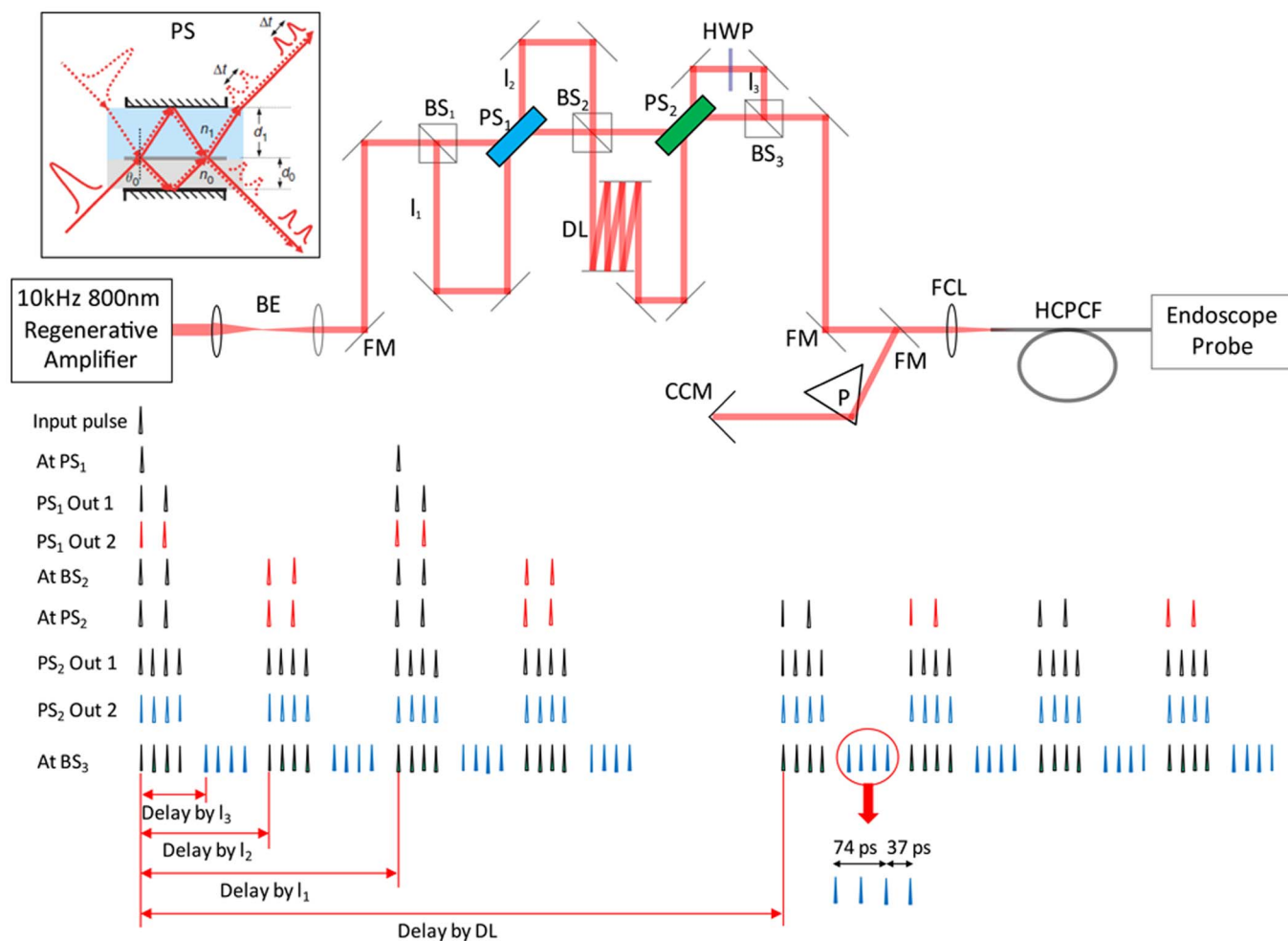


Figure 3 | Schematic diagram of the experimental setup (top) and the timing diagram of the $64\times$ pulse multiplication at each step (bottom). After the pulse splitter, the beam goes through the single prism pulse compressor to compensate the group velocity dispersion induced by HCPCF. The $4\times$ pulse splitter diagram in the box is adapted from the work of Ji *et al.*²⁹, BE: beam expander, FM: flip mirror, BS_{1,2}: non-polarizing beam cube splitter, BS₃: polarizing beam cube splitter, PS₁: pulse splitter with 74 ps pulse separation, PS₂: pulse splitter with 37 ps pulse separation, DL: delay line, HWP: half wave plate, P: prism, CCM: corner cube mirror, FCL: fiber coupling lens, HCPCF: hollow core photonic crystal fiber.

traveled through a different optical path length and were recombined at a beam splitting interface in such a way that the recombined pulses from the output ports of pulse splitter propagated collinearly. After pulse splitting, the pulses were prechirped by the single prism type pulse compressor to compensate for the group velocity

dispersion that may be induced by the intermediate optics and the fiber. Since the separation between the pulses were much smaller than the lifetime of the fluorophores which is typically in the nanoseconds range, the benefit of increasing the repetition rate can only be meaningful when two photon excitation efficiency is low

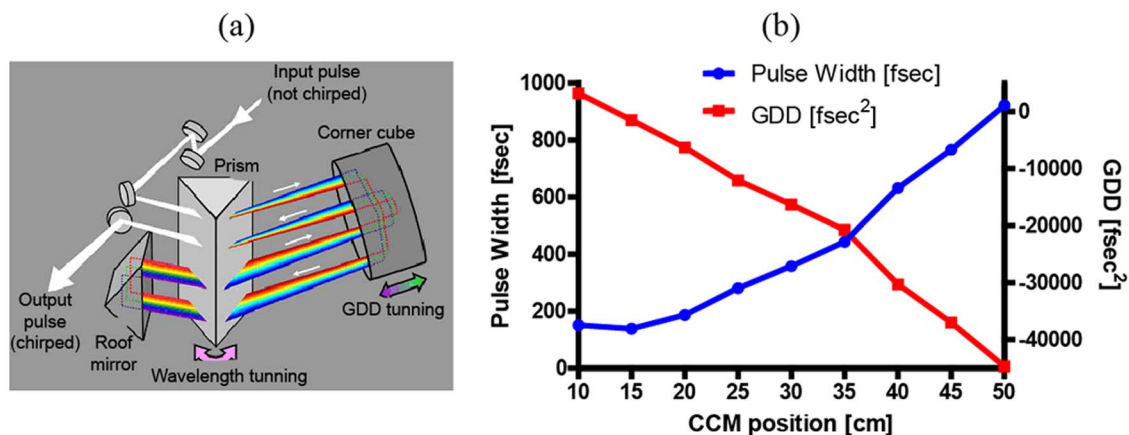


Figure 4 | Single prism pulse compressor for tuning GDD (a) Schematic drawing of single prism pulse compressor adapted from the work of Akturk *et al.*⁴¹. Large tuning range of GDD is achieved by using a prism made of highly dispersive glass, SF66. GDD is tuned by changing the distance between the prism and the corner cube mirror. (b) Measured pulse width as a function of the corner cube mirror position. (blue curve). GDD is calculated using Eq.(2) from the measured pulse width. Input pulse width was 130 fsec².

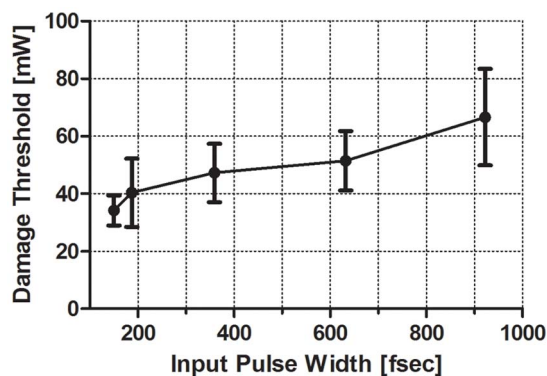


Figure 5 | Damage threshold of HC-800-02 fiber measured without pulse stretching (150 fsec) and with pulse stretching at CCM positions of 20 cm (187 fsec), 30 cm (359 fsec), 40 cm (632 fsec), 50 cm (922 fsec).

enough so that the ground state depletion does not occur as in many cases during temporally focused-wide field two photon imaging. In addition, increasing the repetition rate while decreasing the pulse intensity appropriately can sometimes reduce photodamage and photobleaching while maintaining the same signal level²⁹.

Increasing the damage threshold by stretching the pulse. HCPCF damage typically occurred at the inlet of the fiber where the lattice structure of the air hole and silica surrounding the core was fractured by the strong reaction of the ionized air molecules, generated by the extremely high peak power of the focused beam, with the silica in the fiber cladding. Thus, stretching the pulse to reduce pulse peak energy should allow higher average power to be transmitted before damaging the fiber³⁰.

Pulse width can be controlled by adding negative group delay dispersion (GDD) using a pulse compressor. As shown in Fig. 4, the amount of GDD induced by the pulse compressor is linearly proportional to the distance between the prism and the corner cube mirror (CCM). The pulse width was measured with the single shot autocorrelator (Delta single shot autocorrelator, Minioptic Technology). From the measured pulse width, GDD can be calculated assuming that the shape of the input pulse is in a transform limited Gaussian form³¹. Input pulse width was 130 fsec².

$$GDD = \frac{\tau_{in}}{4 \ln 2} \sqrt{\tau_{out}^2 - \tau_{in}^2} \text{ [fsec}^2\text{]} \quad (2)$$

Damage threshold of HCPCF (HC-800-02, NKT photonics) was measured with the configuration shown in Fig. 3. HC-800-02 had a NA of 0.2, a mode field diameter ($1/e^2$ width) of 5.5 μm and the zero dispersion wavelength near 778 nm. Damage threshold was measured first without pulse stretching and then at four different CCM positions each at 20 cm, 30 cm, 40 cm, 50 cm. The pulse widths at these conditions corresponded to 150 fsec, 187 fsec, 359 fsec, 632 fsec, 922 fsec respectively. At each measurement conditions, the input power was increased at 5 mW increment until the coupling efficiency started to fall; the damage threshold was defined as the power level at which a 10% coupling efficiency drops was observed. At each condition, the measurement was repeated five times. Typical coupling efficiency was 80% which was lower than that without the pulse compressor because the beam shape was slightly elongated horizontally while the beam propagates through the pulse compressor. According to Fig. 5, the damage threshold increased by about factor of two while the input pulse width was increased and the peak power was decreased by about a factor of six. The damage threshold did not increase linearly with an increase in pulse width as expected. This may be caused by the thermal stress built up by the pulses with picosecond time separation since the time constant for the thermal dissipation of HCPCF is on the nanosecond range. Currently, the input pulses from the 10 kHz regenerative amplifier were separated by 100 μsec time delay and this single input pulse was splitted into 64 pulses with 37 psec temporal separation. This issue with thermal stress can be alleviated by separating the pulses more uniformly in between the 10 kHz pulses. This can be achieved with a pulse splitter with much larger overall footprint. A variable repetition rate amplifier is another option that can provide high peak power pulses that are more uniformly spaced in time and may be preferable as these devices will becoming more commercially available.

Although pulse stretching may allow more power to be delivered through the fiber, the long pulse width will decrease the two photon absorption efficiency as predicted by Eq.(1). The solution of this problem is well known. The pulse can be first stretched with negative dispersion provided by the pulse compressor to reduce the ionization effect at the fiber input surface. By choosing a fiber that has positive dispersion at the operating wavelength, the pulse can be restored to the transform-limited by passing through a proper length of HCPCF. Once the beam was coupled to HCPCF, over 95% of the optical power was confined in the air core. Therefore, the material dispersion was minimal and the waveguide dispersion was the dominant factor for the group velocity dispersion induced in the HCPCF³². For 800 nm working wavelength, we choose HC-800-01 for its positive GDD. The GDD of HCPCF (HC-800-01) was calculated from the pulse widths measured before and after the fiber with a chosen length of 80 cm. The input pulse width before fiber was 130 fsec and the pulse width

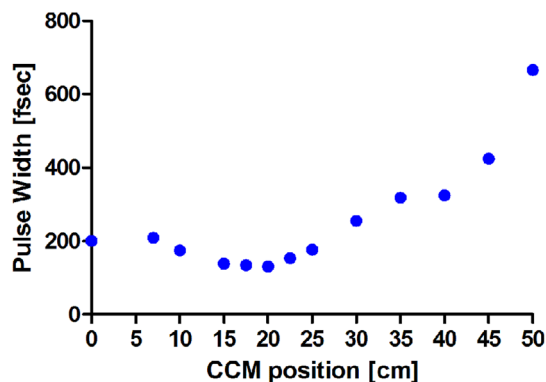


Figure 6 | Pulse width measured after the fiber (HC-800-01) for various amount of negative GDD from the pulse compressor. CCM at 0 cm corresponds to the pulse width measured without the pulse compressor. The minimal pulse width after the fiber is achieved when CCM is at 20 cm position.

after the fiber was 200 fsec corresponding to a GDD of 7000 fsec². This positive GDD of the fiber can be cancelled out by the same amount of negative GDD of the pulse compressor which can be obtained by positioning the CCM of pulse compressor at 20 cm as shown in Fig. 6.

Overall, we combined both ideas of pulse splitting and pulse stretching to improve the high peak power pulse delivery through the fiber. After $64\times$ pulse multiplication, the damage threshold increased to 60 mW through the fiber. After pulse stretching to 187 fs, the damage threshold further increased to 75 mW (Fig. 7).

Design of a temporally focused widefield two photon endomicroscope (TFEM).

Endoscopic implementation of the TFM requires a compact design while maintaining a reasonable field of view and resolution. The form factor of TPE requires the use of micro-lenses as objectives. Currently, the NA of the available micro-lenses is relatively small compared to normal objectives. For example, the highest NA of commercially available microlenses is 0.8 that have been achieved by the compound lens made of a GRIN lens and a plano-convex lens³³. This modest NA limits the achievable depth resolution of a TFEM. Further, to utilize the full NA of the objective, the focal length of the tube lens has to be sufficiently long such that the full spectrum of the excitation beam will span the back aperture of the objective. However, the focal length ratio between the tube lens relative to the objective must be small to ensure a sufficiently large field-of-view. Therefore, the focal length of the focusing lens has to be selected such that both the depth resolution and the field-of-view requirements are satisfied at the same time^{34,35}.

Considering these design criteria, we can derive a simple mathematical relation that needs to be satisfied to achieve the best resolution given limited NA of the objective. The angular spread $\Delta\beta$ of a spectrum with spectral width $\Delta\lambda$ of first order diffraction can be obtained by differentiating the grating equation, assuming the incidence angle is constant³⁶.

$$\Delta\beta = G \sec(\beta)\Delta\lambda \quad (3)$$

where β is the first order diffraction angle, G is the groove frequency. Assuming the paraxial approximation, the width of the focused spot size at the back aperture of the objective is $f\Delta\beta$, where f is the focal length of the tube lens. Therefore, to utilize the full NA of the objective, each design parameters have to be selected to satisfy the following relation

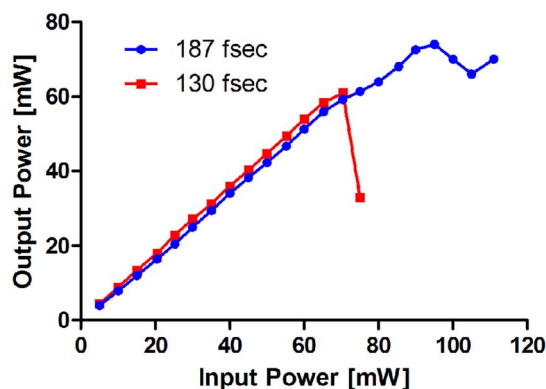


Figure 7 | Damage threshold of the fiber after $64\times$ pulse multiplication without pulse stretching (red) and with pulse stretching (blue).

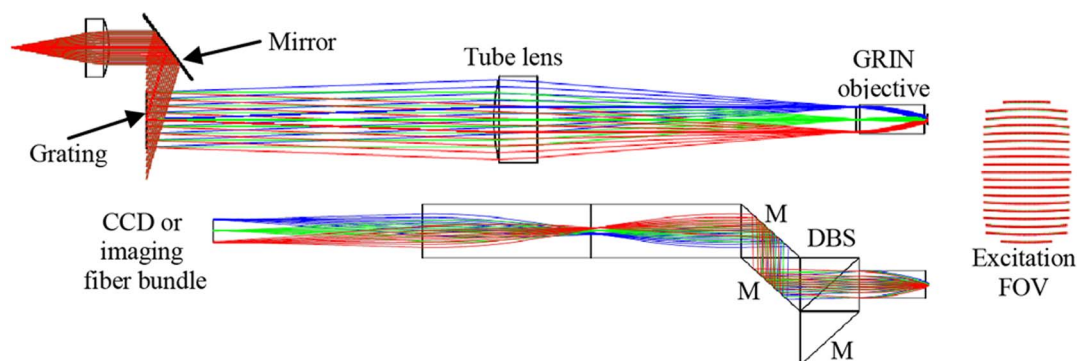


Figure 8 | Optical design of TFEM (top) Ray trace of the excitation beam path. DBS is not shown to better visualize the excitation beam pattern at the back aperture of GRIN objective. Color represents wavelength. (bottom) Ray trace of the emission beam path. Color represents spatial field. Excitation field of view (FOV): $30 \times 60 \mu\text{m}$, Working distance of objective: $180 \mu\text{m}$, NA of objective: 0.8, All ray tracing is performed by commercial software (Zemax, Radiant Zemax), DBS: dichroic beam splitter cube where the excitation light is reflected and the emission light is transmitted, M: Mirror-coated prism.

$$D = fG \sec(\beta) \Delta\lambda \quad (4)$$

where D is the diameter of the back aperture of the objective.

Figure 8 shows the ray tracing of both excitation and emission beam path of a realization of TFEM. Excitation beam was delivered through HCPCF (HC-800-01, NKT photonics) and collimated by plano-convex lens (NT65-308, Edmund Optics, $f = 2.54 \text{ mm}$, $\text{Ø} 2 \text{ mm}$) and reflected by the prism (NT45-524, Edmund Optics) with the custom gold mirror coating (Evaporated Coatings) to a reflective grating (1200 line/mm, $2 \text{ mm} \times 2 \text{ mm}$, LightSmyth). The grating was custom-made so that the first order diffraction was maximized for the excitation wavelength at 800 nm . The input pulses were spectrally dispersed by the grating and focused by a plano-convex lens (Edmund Optics, NT45-964, $f = 12 \text{ mm}$, $\text{Ø} 3 \text{ mm}$) at the back aperture of custom-made GRIN objective (NA 0.8, GRINTECH) that collimated each spectral component and recombined them at the focal plane of the objective to restore original input pulse width. The fluorescence signals from the focal plane were collected by the GRIN objective and relayed through the dichroic beam splitter cube block and the custom-made GRIN imaging lens (GRINTECH) and detected by a $1/10''$ size CCD camera (SEN103670X, FORT-fr) at the distal end directly or can be relayed to the high sensitivity detectors such as EMCCD camera through the imaging fiber bundle (IGN08/30, Sumitomo Electric) located at the proximal end. Depth scanning can be accomplished by tuning the group velocity dispersion at the proximal end as proposed and demonstrated by Durst *et al.*⁷. In this way, all the scanning actuators at the distal end can be removed, resulting in a compact and robust endomicroscope. The optical components were assembled in the custom-made endoscope housing as shown in Fig. 9 with a total form factor of 8 mm in diameter and 35 mm in length.

Results

Experimental validation of the pulse delivery methods. The proposed pulse delivery method for TFEM imaging was validated experimentally by comparing the two-photon excited fluorescence signals of the fluorescent beads in three different cases. In the first case, pulses from 10 kHz regenerative amplifier was delivered directly without pulse multiplication or dispersion compensation. In the second case, each pulse was multiplied 64 times without dispersion compensation. In the third case, a pulse was multiplied

64 times with dispersion compensation. The excitation beam for these conditions were delivered through the fiber (HC-800-01) to a temporally focused widefield two photon endoscope probe. The power levels after the fiber delivery were 2.5 mW , 50 mW , 50 mW respectively. These values were obtained when the input power to the fiber was set to about 70% of the damage threshold to prevent the fiber damage during long-term imaging process. The emission signal was detected in transmission mode with $40\times$ air objective and the EMCCD camera (iXon 885, Andor) placed on the opposite side of the illumination beam path.

The two photon signal was compared using a sample consisting of densely packed $1 \mu\text{m}$ fluorescent beads (F-13081, Molecular Probes) sandwiched between two cover slips. The image was acquired at 100 msec exposure time and repeated 10 times for each condition. Fig. 10(a) shows the normalized total fluorescence signal summed for the whole field of view. Compared to case 1, the signal level increased a factor of 7.5 in case 2 and a factor of 11.5 in case 3. In case 2, while the repetition rate was increased to 64 times, the peak power of the pulse was reduced to $1/3$ compared to case 1. Since the two photon fluorescence signal per second has a quadratic dependence on the peak power and a linear dependence on the repetition rate, about 7 fold increase can be expected. In case 3, the positive pulse dispersion by the fiber was compensated by the negative GDD of the pulse compressor so that the output pulse width of 187 fsec in case 2 was restored to its original pulse width of 130 fsec as shown in Fig. 6. Since the two photon absorption (TPA) was inversely proportional to the pulse width, about 1.4 fold increase in two photon signal can be expected. Therefore, by using the pulse splitter and dispersion compensation (case 3) 11.5 fold increase in two photon signal have been achieved. This effect was also verified in Fig. 10 (b)–(d) where $2 \mu\text{m}$ fluorescent bead (F-8827, Molecular Probes) was imaged at

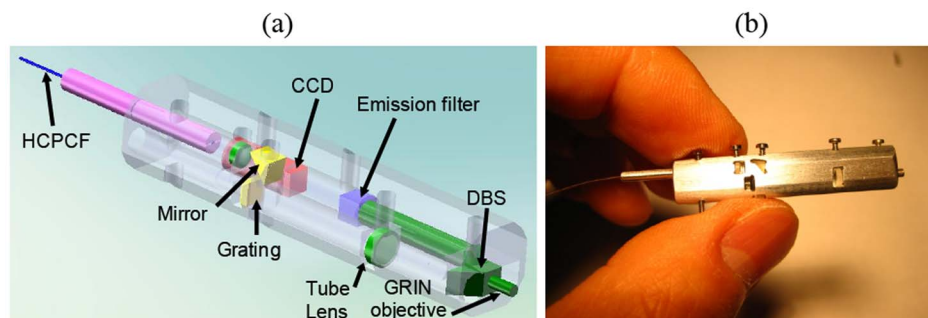


Figure 9 | Assembled TFEM showing the endoscope housing and the optical components (a) 3D modeling. (b) Fabricated TFEM. Size: 8 mm (diameter), 35 mm (length).

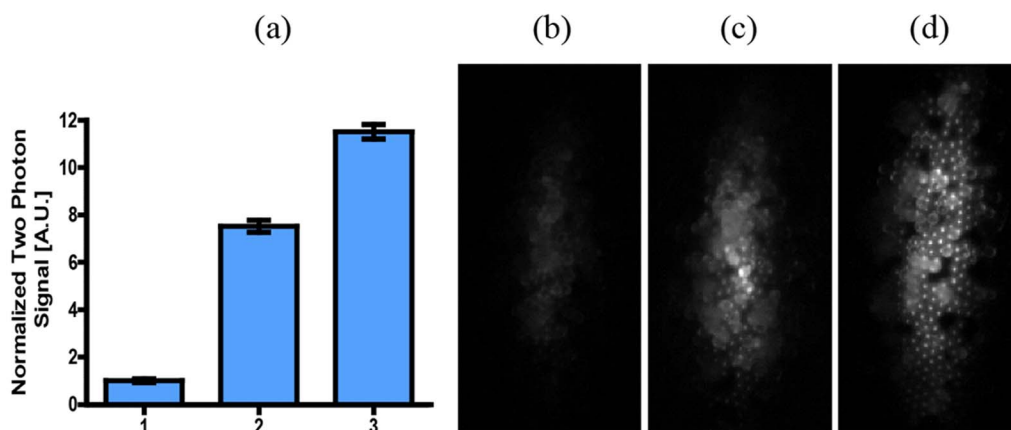


Figure 10 | Comparison of the two photon signal by three different pulse delivery methods (a) Normalized two photon signal for three cases. 1. No pulse multiplication without dispersion compensation 2. With $64\times$ pulse multiplication and without dispersion compensation 3. With $64\times$ pulse multiplication and dispersion compensation (b), (c), (d) are $2\ \mu\text{m}$ bead images for case 1, 2 and 3 respectively. The emission signal is detected in transmission mode with $40\times$ air objective and the EMCCD camera (iXon 885, Andor) placed on the opposite side of the illumination beam path.

each conditions. The field of view was quite elongated vertically because the input angle of the excitation beam to the grating surface was 73° . The FOV can be made square by expanding the beam horizontally with two cylindrical lens pair before impinging on the grating.

Discussion

This paper presents an improved delivery method of high peak power laser pulses from a regenerative amplifier through a hollow core photonic crystal fiber to maximize two photon excited fluorescence signal in a temporally focused wide-field two photon endomicroscopy.

Signal improvement has been demonstrated by using a pulse splitter that divides a single pulse into 64 pulses that have a peak power level that is just below the fiber damage threshold. The fiber damage threshold can be further increased by stretching the pulses with negative GDD using a pulse compressor resulting in low peak power at the fiber inlet. This negative GDD is precisely compensated by the positive GDD of a specific length of fiber resulting in the recompression of the pulse to its original width at the fiber outlet. By employing the pulse multiplication and the dispersion compensation in TFEM, 11 fold signal increase have been demonstrated.

If we assume that thermal stress plays a role in fiber damage, a variable repetition rate regenerative amplifier should provide more flexibility in finding the optimal pulse energy and repetition rate that maximize the TPA signal while preserving fiber integrity. The damage of the fiber occurs in most cases at the inlet of the fiber where the delicate lattice structure around the air core can be fractured by the high intensity focused beam. Recent development in fiber end treatment technology has a great potential that can increase the damage threshold by collapsing the end face and hermetically sealing the fiber³⁷. In this way, the lattice structure would not be directly in contact with air and should reduce the damage possibility by ionization. Also, since the input beam is guided to the core by refraction when passing through the collapsed area, the beam size at the end face can be made larger effectively increasing the damage threshold by reducing beam intensity at the end face.

There are also many opportunities for improving the endoscope design. The currently available high NA GRIN lens was not well corrected for the chromatic aberration, causing each spectral component to be focused at different position in axial position resulting in pulse broadening with lower TPA efficiency. This limitation may be overcome using custom-designed micro-optics compound lens¹³. The power loss within the endoscope mostly occurred at the grating. To reduce the length of the endoscope size, a high groove density

grating with 1200 line/mm was used in the current design. The power loss was significant and only 15% of input power was diffracted to the first order beam. The current design may be improved with an alternative approach that utilizes grating with lower groove density and more optimized brazing angle. The current design of the endoscope was 8 mm in diameter. A more compact design may be achieved by using a GRISM such that the excitation beam path can be made straight in-line without the need for beam steering mirror^{38,39}. Finally, the GDD was tuned by manually translating the corner cube mirror in the pulse compressor. Faster axial scanning may be achieved by tuning the GDD using a piezo bimorph mirror⁴⁰.

- Denk, W., Strickler, J. H. & Webb, W. W. Two-photon laser scanning fluorescence microscopy. *Science* **248**, 73–76 (1990).
- Huang, D. *et al.* Optical Coherence Tomography. *Science* **254**, 1178–1181 (1991).
- Xu, M. H. & Wang, L. H. V. Photoacoustic imaging in biomedicine. *Rev. Sci. Instrum.* **77**, 041101 (2006).
- Skala, M. C. *et al.* In vivo multiphoton microscopy of NADH and FAD redox states, fluorescence lifetimes, and cellular morphology in precancerous epithelia. *P. Natl. Acad. Sci. U.S.A.* **104**, 19494–19499 (2007).
- Skala, M. C. *et al.* Multiphoton microscopy of endogenous fluorescence differentiates normal, precancerous, and cancerous squamous epithelial tissues. *Cancer Res.* **65**, 1180–1186 (2005).
- Nadiarynkh, O., LaComb, R. B., Brewer, M. A. & Campagnola, P. J. Alterations of the extracellular matrix in ovarian cancer studied by Second Harmonic Generation imaging microscopy. *BMC Cancer* **10**, 14 (2010).
- Tai, D. C. S. *et al.* Fibro-C-Index: comprehensive, morphology-based quantification of liver fibrosis using second harmonic generation and two-photon microscopy. *J. Biomed. Opt.* **14**, 10 (2009).
- Zhang, Y. Y. *et al.* A compact fiber-optic SHG scanning endomicroscope and its application to visualize cervical remodeling during pregnancy. *P. Natl. Acad. Sci. U.S.A.* **109**, 12878–12883 (2012).
- Myaing, M. T., MacDonald, D. J. & Li, X. D. Fiber-optic scanning two-photon fluorescence endoscope. *Opt. Lett.* **31**, 1076–1078 (2006).
- Bao, H. C., Allen, J., Pattie, R., Vance, R. & Gu, M. Fast handheld two-photon fluorescence microendoscope with a $475\ \mu\text{m} \times 475\ \mu\text{m}$ field of view for in vivo imaging. *Opt. Lett.* **33**, 1333–1335 (2008).
- Le Harzic, R., Weinigel, M., Riemann, I., Konig, K. & Messerschmidt, B. Nonlinear optical endoscope based on a compact two axes piezo scanner and a miniature objective lens. *Opt. Express* **16**, 20588–20596 (2008).
- Liu, G. J. *et al.* Rotational multiphoton endoscopy with a $1\ \mu\text{m}$ fiber laser system. *Opt. Lett.* **34**, 2249–2251 (2009).
- Wu, Y. C., Xi, J. F., Cobb, M. J. & Li, X. D. Scanning fiber-optic nonlinear endomicroscopy with miniature aspherical compound lens and multimode fiber collector. *Opt. Lett.* **34**, 953–955 (2009).
- Rivera, D. R. *et al.* Compact and flexible raster scanning multiphoton endoscope capable of imaging unstained tissue. *P. Natl. Acad. Sci. U.S.A.* **108**, 17598–17603 (2011).
- Oron, D., Tal, E. & Silberberg, Y. Scanningless depth-resolved microscopy. *Opt. Express* **13**, 1468–1476 (2005).
- Zhu, G. H., van Howe, J., Durst, M., Zipfel, W. & Xu, C. Simultaneous spatial and temporal focusing of femtosecond pulses. *Opt. Express* **13**, 2153–2159 (2005).



17. Durst, M. E., Zhu, G. H. & Xu, C. Simultaneous spatial and temporal focusing for axial scanning. *Opt. Express* **14**, 12243–12254 (2006).
18. Cheng, L. C. *et al.* Spatiotemporal focusing-based widefield multiphoton microscopy for fast optical sectioning. *Opt. Express* **20**, 8939–8948 (2012).
19. Russell, P. Photonic crystal fibers. *Science* **299**, 358–362 (2003).
20. Couny, F., Benabid, F., Roberts, P. J., Light, P. S. & Raymer, M. G. Generation and photonic guidance of multi-octave optical-frequency combs. *Science* **318**, 1118–1121 (2007).
21. Kim, D., Choi, H., Yazdanfar, S. & So, P. T. C. Ultrafast Optical Pulse Delivery With Fibers for Nonlinear Microscopy. *Microsc. Res. Techniq.* **71**, 887–896 (2008).
22. Tai, S. P. *et al.* Two-photon fluorescence microscope with a hollow-core photonic crystal fiber. *Opt. Express* **12**, 6122–6128 (2004).
23. Shephard, J. D. *et al.* Improved hollow-core photonic crystal fiber design for delivery of nanosecond pulses in laser micromachining applications. *Appl. Optics* **44**, 4582–4588 (2005).
24. Konorov, S. O. *et al.* Hollow-core photonic-crystal fibres for laser dentistry. *Phys. Med. Biol.* **49**, 1359–1368 (2004).
25. Ishaaya, A. A. *et al.* Highly-efficient coupling of linearly- and radially-polarized femtosecond pulses in hollow-core photonic band-gap fibers. *Opt. Express* **17**, 18630–18637 (2009).
26. Wang, Y. Y. *et al.* Design and fabrication of hollow-core photonic crystal fibers for high-power ultrashort pulse transportation and pulse compression. *Opt. Lett.* **37**, 3111–3113 (2012).
27. Horton, N. G. *et al.* In vivo three-photon microscopy of subcortical structures within an intact mouse brain. *Nat. Photonics* **7**, 205–209 (2013).
28. Kienel, M. *et al.* Energy scaling of femtosecond amplifiers using actively controlled divided-pulse amplification. *Opt. Lett.* **39**, 1049–1052 (2014).
29. Ji, N., Magee, J. C. & Betzig, E. High-speed, low-photodamage nonlinear imaging using passive pulse splitters. *Nat. Methods* **5**, 197–202 (2008).
30. Wang, T. H., Kumavor, P. D. & Zhu, Q. Application of laser pulse stretching scheme for efficiently delivering laser energy in photoacoustic imaging. *J. Biomed. Opt.* **17**, 061218 (2012).
31. Wokosin, D. L. Pulse duration spectra and measurements for laser scanning microscope systems. *Proc. Spie* **5700**, 1–13 (2005).
32. Saleh, B. E. A. & Teich, M. C. *Fundamentals of photonics*. 2nd edn, (John Wiley & Sons, 2007).
33. Messerschmidt, B. *et al.* Novel concept of GRIN optical systems for high resolution microendoscopy. Part 1: Physical aspects - art. no. 643202. *Proc. Spie* **6432**, 43202–43202 (2007).
34. Kim, D. & So, P. T. C. Three-Dimensional (3D) High-Speed Imaging and Fabrication System Based on Ultrafast Optical Pulse Manipulation. *Proc. Spie* **7183**, 71831B (2009).
35. Dana, H. & Shoham, S. Numerical evaluation of temporal focusing characteristics in transparent and scattering media. *Opt. Express* **19**, 4937–4948 (2011).
36. Palmer, C. & Loewen, E. *Diffraction grating handbook*. 6th edn, (Newport, 2005).
37. *Photonic crystal fiber end-sealing*. (NKT Photonics).
38. Pitris, C., Bouma, B. E., Shiskov, M. & Tearney, G. J. A GRISM-based probe for spectrally encoded confocal microscopy. *Opt. Express* **11**, 120–124 (2003).
39. Dana, H. & Shoham, S. Remotely scanned multiphoton temporal focusing by axial grism scanning. *Opt. Lett.* **37**, 2913–2915 (2012).
40. Straub, A., Durst, M. E. & Xu, C. High speed multiphoton axial scanning through an optical fiber in a remotely scanned temporal focusing setup. *Biomed. Opt. Express* **2**, 80–88 (2011).
41. Akturk, S., Gu, X., Kimmel, M. & Trebino, R. Extremely simple single-prism ultrashort-pulse compressor. *Opt. Express* **14**, 10101–10108 (2006).

Acknowledgments

This work was supported by NIH 9P41EB015871-26A1, 5R01EY017656-02, 5R01NS051320, 4R44EB012415-02, NSF CBET-0939511, the Singapore-MIT Alliance 2, the Singapore-MIT Alliance for Science and Technology Center (BioSymb IRG), the MIT SkolTech initiative, the Hamamatsu Corp. and the Koch Institute for Integrative Cancer Research Bridge Project Initiative.

Author contributions

H.C. and P.S. designed and performed the experiments, analysed data and wrote the paper.

Additional information

Competing financial interests: The authors declare no competing financial interests.

How to cite this article: Choi, H. & So, P.T.C. Improving femtosecond laser pulse delivery through a hollow core photonic crystal fiber for temporally focused two-photon endomicroscopy. *Sci. Rep.* **4**, 6626; DOI:10.1038/srep06626 (2014).



This work is licensed under a Creative Commons Attribution-NonCommercial-NoDerivs 4.0 International License. The images or other third party material in this article are included in the article's Creative Commons license, unless indicated otherwise in the credit line; if the material is not included under the Creative Commons license, users will need to obtain permission from the license holder in order to reproduce the material. To view a copy of this license, visit <http://creativecommons.org/licenses/by-nc-nd/4.0/>